Origin of the gypsum veins associated with the diagenetic dolomite nodules from the Neogene Marls of South-East Spain

Catherine Pierre, Jean-Marie Rouchy

Origin of the Gypsum Veins Associated with the Diagenetic Dolomite Nodules from the Neogene Marls of South-East Spain.

Catherine Pierre[1] and Jean-Marie Rouchy[2]

1 LOCEAN-IPSL, CNRS-IRD-MNHN, Sorbonne Université, 4 Place Jussieu, 75252 Paris Cedex 05, France

catherine.pierre@locean.upmc.fr

2 Géologie, Muséum National d'Histoire Naturelle, 43 rue Buffon, 75005, Paris, France

Abstract

The late Neogene marls from the Lorca, Murcia and Vera basins in S-E. Spain contain abundant dolomite nodules that were formed due to intense methane-rich fluid migration. The pathways for these fluids are evidenced by dense networks of fractures that are crossing the sedimentary layers and eventually the dolomite nodules. The fractures are generally filled by secondary fibrous gypsum that form veins of a few cm thick.

The oxygen and sulfur isotopic compositions of the gypsum veins exhibit wide ranges (-2.2 < $\delta^{18}O‰$ VSMOW < 6.7 ; -22.3 < $\delta^{34}S‰$ VCDT< 10.5) that are far away from the average δ values of Tortonian-Messinian gypsum from the basins of Lorca, Fortuna and Sorbas ($\delta^{18}O$ = 13.8 ± 2.3‰; $\delta^{34}S$ = 21.3 ± 1.0‰) precipitated from the late Neogene seawater sulfate. These low δ values of the gypsum veins clearly indicate their diagenetic origin that would have resulted from sulfide oxidation with ^{18}O-depleted water. The isotopic compositions of the diagenetic dolomite nodules close to the gypsum veins (-0.7 < $\delta^{18}O‰$ VPDB < 3.7; -11.9 < $\delta^{13}C‰$ VPDB < 7.3) are indicative of their formation in methane-rich fluids. In this context, the formation of sulfide is related to the bacterial sulfate reduction that is associated with the anaerobic oxidation of methane. During this process, pyrite coprecipitated with dolomite, either within the dolomite framework or within conduits where the fluids were seeping. The pyrite oxidation occurred later during diagenesis when more or less oxygenated groundwaters circulated within the fractures during the sealevel

drawdown of the Messinian Salinity Crisis and after the regional uplift of the sedimentary deposits in relation with the Betic cordillera tectonics.

1. Introduction

The Tortonian, Messinian and lower Pliocene marls outcropping in S.E. Spain basins are predominantly located in the internal zone of the Betic cordillera (Murcia, Aledo, Lorca, Sorbas, Huercal Overa, Albox, Vera) or at the transition between the internal and external zones (Fortuna) (Fig. 1). They contain abundant authigenic dolomite nodules. Previous studies of these authigenic carbonates (Pierre and Rouchy, 2004; Pierre et al., 2002, 2015, 2018) have shown that they were precipitated within the marly sediments due to circulation of fluids of various origin and composition that are recorded by the large variability of the isotopic values ($-7.9 < \delta^{18}O‰$ VPDB < 6.3; $-35.5 < \delta^{13}C‰$ VPDB < 9.8). These authigenic carbonates are thus considered as archives of the past history of fluid migration during at least 11 Ma. During this long period where major paleoenvironmental and tectonic changes occurred in the Mediterranean domain (the successive tectonic events from the formation of the Neogene basins up to their final uplift, the Messinian salinity crisis), these fluids were largely modified by different processes: gas hydrate formation/dissociation, clay minerals dehydration, evaporitic brines, deep-warm fluids, anaerobic oxidation of methane, methanogenesis.

In some places the sedimentary series containing the dolomite nodules are intensely faulted and the veins are often infilled with secondary gypsum (Fig. 2A). Secondary gypsum may also occur around and within the dolomite nodules (Figs. 2B, C, D, E). Similar occurrences of dolomite nodules related to diagenesis with methane-rich fluids have also been described in many outcrops, e.g.: the Eocene of North-East Spain (Hoareau et al., 2008), the late Neogene of Northern Apennines and Piedmont in Italy (Dela Pierre et al, 2010; Oppo et al., 2017), the Miocene of New Zealand (Nyman et al., 2010), the Miocene of California (Aiello et al., 2001). These dolomite structures are sometimes associated with secondary veins of celestite, barite and calcite but never with secondary gypsum veins.

In the geological context of the S.E. Spain basins during Neogene, the possible relationship of the secondary gypsum veins with the Tortonian-Messinian evaporites, either by circulation of sulfate-rich solutions issued from dissolution of gypsum deposits or from connate brines, might be questionned. The determination of the origin of the secondary gypsum veins by oxygen and sulfur stable isotopes ($\delta^{18}O$ and $\delta^{34}S$) would thus provide the

clue to bring a better knowledge of the composition and origin of the fluids that were circulating either within the fault networks or percolating through the microfractures and porosity of the sediments.

2. Geological background

The Betic Cordillera constitutes the northern arm of the Betic-Rifian arcuate belt, which is the westernmost part of the Alpine orogen issued from the collision of the African and Eurasian plates. It is usually divided into an external zone composed of deformed Mesozoic to Tertiary sediments initially deposited on the southern margin of Iberia and an Internal Zone made of a pile of nappes composed of Paleozoic to Mesozoic rocks affected by different degrees of metamorphism (Fig. 1). The Albox, Vera, Lorca and Murcia basins where the studied samples have been collected, belong to a complex system of interconnected intramontane basins that formed after the cessation of the westward drift of the Internal Zones that occurred towards the end of the middle Miocene, and in relation with the development of SW-NE strike-slip fault zones as the Alhama de Murcia faults which extend from Huercal Overa to Alicante and the Palomares faults located in the Almeria-Vera area (Montenat et al., 1987; de Larouzière et al., 1988; Sanz de Galdeano, 1990, 1992) (Fig.1). The most common characteristic of these basins was the intense subsidence with high sedimentation rates during the Tortonian. However, their paleogeography and sedimentary settings evolved differently until the Quaternary under a complex control involving not only the variation of activity of these fault systems under a predominantly compressional regime with episodes of distension (Sanz de Galdeano, 1990; Sanz de Galdeano and Vera, 1992), but also their position within the organisation of the Betic substrate and their proximity to the deep central Mediterranean Basin. Accordingly, the major subsidence and the final uplift ending by the withdrawal of the sea may differ strongly from a basin to another.

In the Vera and Murcia basins, which occupied the more proximal position with regard to the deep Mediterranean, marine conditions persisted through the whole Tortonian until the early Pliocene (Fig. 3). The Messinian Salinity Crisis impacted directly these two basins with deposition of gypsum in the eastern part of the Murcia Basin (San Miguel de Salinas area) and in the Vera Basin where it has been removed as a megabreccia during the final drawdown of the Mediterranean sea level responsible, in the two basins, for an important erosional surface at the Messinian/Zanclean transition (Montenat et al., 1976, 1977; Pierre et al., 2006; Corbí et al., 2016; Caruso et al., 2020) (Fig. 3). In the Albox basin located at the SW end of the

93 Alhama de Murcia fault system, marine deposition ceased at the end of Tortonian in response
94 to tectonic uplift, the last Messinian marine deposits being known only in the nearby Huercal
95 Overa basin to the east (Guerra-Merchán and Serrano, 1993; Meijninger and Vissers, 2006;
96 Pedrera et al., 2010). The Lorca basin close to the boundary with the External Zones had a
97 more complex sedimentary evolution. It underwent an earlier marine restriction during late
98 Tortonian/early Messinian responsible for the deposition of a sequence composed of silicified
99 dolostones grading upward into an organic-rich diatomite-bearing unit and finally to an
100 evaporitic (gypsum and salt) unit (Rouchy et al., 1998; Krijgsman et al., 2006; Playà et al.,
101 2000), (Figs. 2F, 3).

102 ## 2. Material and methods

103 ### 2.1 Gypsum veins

104 In the basins of Murcia, Lorca, Vera, Albox, as in most of the other basins, the
105 dolomite nodules are associated to secondary gypsum that exhibits a wide range of size,
106 morphologies and distribution through the marls and the nodules. These gypsum occurrences
107 commonly appear as veins cm to dm in thickness and up to several meters of length that cut
108 the marls perpendicularly, obliquely or more or less conformably to the bedding of the host
109 sediment and making sometimes a dense network (Fig. 2A). The gypsum veins may also cut
110 irregularly the nodules themselves or form an external envelope around them (Figs. 2B, C, D).
111 Locally, a nodule is crossed by a polygonal network of fissures looking like septarian cracks
112 (Fig. 2B). The gypsum may also display micronodular shapes disseminated within the
113 carbonate nodules or aggregates of larger selenitic crystals, several cm in size filling the
114 central part of nodules (Fig. 2E). In the Lorca basin, the stratigraphic interval containing the
115 nodules ends with a succession of well-stratified beds several dm-thick of opal-CT rich
116 dolostones intercalated with gypsum veins associated with alunite [$(Na,K)\ Al_3\ (SO_4)_2\ (OH)_6$]
117 occurences (Fig. 2F).

118 Eight gypsum samples were collected in the marly deposits that contain also abundant
119 authigenic dolomite nodules, from the late Neogene (Late Tortonian to early Pliocene) of the
120 basins of Lorca, Albox, Murcia and Vera (Table 1). In the Murcia Basin, two sets of samples
121 were collected in the early/middle Tortonian (ES 16.125, ES 16.126, ES 16.127) and near the
122 Tortonian/Messinian transition (ES 17.45, ES 17.46, ES 17.64) along the road between
123 Cabezo de la Plata and Los Ginovinos (Fig. 3). In the Vera basin, the samples come from the
124 early Pliocene (Zanclean) marls located near the Vera graveyard, and at Albox from

Tortonian levels in the Olleres oucrops (Fig. 3). In the Lorca Basin, the samples were taken into interval of dolomitic nodules and cherty dolostones and in the overlying organic-rich deposits of the diatomite-bearing unit that crop out in the La Serrata section at the transition between the Tortonian marine marls and the massive gypsum unit (Fig. 3). The gypsum samples generally exhibit fibrous satin-spar lithofacies where the gypsum crystals are oriented perpendicular to the walls of the veins (Rouchy et al., 1994). This facies is characteristic of secondary precipitation of gypsum from circulation of saturated solutions in open fractures.

Prior to stable isotope analyses, gypsum was converted to $BaSO_4$ following the classical procedure described by Longinelli and Craig (1967). Gypsum was dissolved in acidified dionized water; the resulting solution was then filtered (0.8 µm), heated and barium sulfate was precipitated by adding a 1N-$BaCl_2$ solution. The $BaSO_4$ precipitate was finally filtered, rinced with deionized water and dried in an oven at 90°C. Oxygen isotope analyses were conducted on a ThermoScientific Delta V Advantage IRMS at LOCEAN, Sorbonne Université, Paris. The IRMS is coupled with a Conflo IV interface and Flash-EA2000 (Thermal Conversion Elemental Analyzer Unit) where pyrolysis (at 1400°C) and combustion (at 1050°C) produce CO and SO_2 for oxygen and sulfur isotopic analyses, respectively. For pyrolysis, about 150µg of $BaSO_4$ plus 1 mg of AgCl (Boschetti and Iacumin, 2005) are weighted and pressed in a silver capsule. For combustion, about 250µg of $BaSO_4$ plus 1 mg of V_2O_5 are weighted and pressed in a tin capsule.

The $\delta^{18}O$ and $\delta^{34}S$ values were calibrated using the IAEA international references [(NBS 127 : $\delta^{18}O$ = +8.5±0.2‰ VSMOW, Boschetti and Iacumin, 2005; $\delta^{34}S$ = +21.2 ±0.2‰ VCDT, Halas and Szaran, 2001), (S1 : $\delta^{34}S$ = -0.3‰ VCDT), (S2 : $\delta^{34}S$ = +22.7‰ VCDT), (S3 : $\delta^{34}S$ = -32.3‰ VCDT)].

The oxygen and sulfur isotopic compositions are expressed in the δ notation :

$$\delta = (R_{sample}/R_{reference} - 1) \times 1000$$

where R = $^{18}O/^{16}O$ or $^{34}S/^{32}S$ in the sample and in the reference, using the international reference VSMOW (Vienna Standard Mean Ocean Water) and VCDT (Vienna Cañon Diablo Troilite) for $\delta^{18}O$ and $\delta^{34}S$ measurements respectively. The analytical precision is ±0.2‰ for $\delta^{18}O$ and $\delta^{34}S$ measurements.

2.2 Dolomite nodules

155 The dolomite nodules associated to the gypsum veins exhibit the common facies of
156 rounded to elongated massive compact bodies, which diameter generally of a few decimeters
157 may reach up to more than one meter (Figs. 2 B, C, D, E). The bulk mineralogy of the nodules
158 was determined by XRD and was completed by SEM observations of the morphology and
159 composition of the crystals (Fig. 4).

160 The oxygen and carbon isotopic compositions of dolomites were determined on the
161 bulk powdered samples. A fraction of about 100 to 200 µg was reacted at 90°C with
162 orthophosphoric acid using a multicarb system coupled with a dual inlet isotopic ratio mass
163 spectrometer (DI IRMS) VG Isoprime. The $\delta^{18}O$ values reported in Table 1 were corrected for
164 the phosphoric acid fractionation at 90°C (Rosenbaum and Shepard (1986). The analytical
165 precision 2σ is 0.01‰ and the reproducibility is ±0.2‰ for both $\delta^{18}O$ and $\delta^{13}C$ values.

166 The oxygen and carbon isotopic compositions are expressed in the δ notation where R =
167 $^{18}O/^{16}O$ or $^{13}C/^{12}C$ in the sample and in the reference, using the international reference VPDB
168 (Vienna Peedee Belemnitella) defined by Craig (1957) and revised by Gonfiantini et al.
169 (1995).

170 3. Results

171 3.1 Gypsum veins

172 The microscopic SEM observations of gypsum veins show their internal fabrics where
173 the gypsum crystals exhibit generally platy and fibrous habits (Figs. 4A, B) and include
174 numerous sedimentary particles (detrital silicates, coccolites, calcite and dolomite aggregates)
175 that were cemented during gypsum precipitation. The sedimentary inclusions also contain
176 previous pyrite structures of framboids and octahedra, that are still present but as oxidized Fe-
177 products (Figs. 4C, D, E, F). These occurrences confirm that bacterial sulfate reduction was
178 responsible for pyrite formation during early diagenesis when methane-rich fluids circulated
179 within the sedimentary matrix. Further circulation of oxygenated waters through the
180 sedimentary deposits led to pyrite oxidation that was converted to Fe-oxy-hydroxides and
181 produced sulfate-rich acid solutions from which carbonates were dissolved and gypsum was
182 precipitated. Calcite and dolomite dissolution is evidenced by numerous holes within the
183 crystals (Fig. 4F)

The $\delta^{18}O$ and $\delta^{34}S$ values of the gypsum veins (Table 1; Fig. 5) vary in large ranges (-2.2< $\delta^{18}O$‰ VSMOW< 6.7 ; -22.3 < $\delta^{34}S$‰ VCDT< 10.5). The highest $\delta^{34}S$ value is measured in the gypsum of Lorca that is associated with alunite. However, all these values are much lower than those of the Tortonian-Messinian marine gypsum from the SE Spain basins of Sorbas, Lorca and Fortuna ($\delta^{18}O$ = 13.8 ± 2.3‰ VSMOW ; $\delta^{34}S$ = 21.3 ± 1.0‰VCDT ; Evans et al., 2015; Garcia-Veigas et al., 2019).

3.2 Dolomite nodules

The SEM observations (Figs. 6A, B, C, D) reveal that the dolomite rhombs are always associated with pyrite (mostly as framboids) that may be preserved or oxidized. In some cases, dolomite rhombs show numerous cavities that correspond probably to dissolved pyrite that was included within the dolomite crystals (Fig. 6B).

The $\delta^{18}O$ and $\delta^{13}C$ values of the dolomite nodules (Table 1, Fig. 7) vary also in wide ranges (-0.7 < $\delta^{18}O$‰ VPDB < 3.7 ; -11.9 < $\delta^{13}C$‰ VPDB < 7.3) that display distinct groups between Vera (with the lowest $\delta^{13}C$ values), Murcia and Lorca (with the lowest $\delta^{18}O$ values and the highest $\delta^{13}C$ values) and Albox (with the highest $\delta^{18}O$ values).

4. Discussion

The precipitation of the authigenic minerals (dolomite, pyrite, secondary gypsum, alunite, silica) was controlled by biogeochemical reactions related to complex processes where reducing and oxidizing conditions were occuring at different stages of diagenesis (Fig. 8). The isotopic compositions recorded by dolomite and gypsum are indicative of important variations of the composition of the diagenetic fluids that were involved during their precipitation.

4.1 The biogeochemical reactions under anoxic conditions

4.1.1 Dolomite diagenesis

The production of dissolved inorganic carbon (DIC) in pore fluids occurs when anoxic conditions in organic-rich sediments enhance microbial activity, which controls also the cycling of other elements as sulfur and iron (Konhauser, 2007). Because organic matter is depleted in ^{13}C ($\delta^{13}C$~-25‰), the products of its degradation (biogenic and thermogenic) are also depleted in ^{13}C, especially the most common gas product, CH_4, which has $\delta^{13}C$ values

213 varying between -110 and -30‰ (Claypool and Threlkeld, 1983; Whiticar, 1999). During
214 methanogenesis, there is a large isotopic fractionation between the two by-products CH_4 and
215 CO_2, which gives ^{13}C-poor CH_4 and ^{13}C-rich CO_2 (Whiticar and Faber, 1986; Alperin et al.,
216 1988). In such context, ^{13}C-depleted DIC is released during microbial reduction of sulfate
217 with methane (or heavier hydrocarbons), whereas ^{13}C-rich DIC is produced during
218 methanogenesis (Fig. 8). The recent review by Meister and Reyes (2019) of the carbon
219 isotope variations in marine environments summarizes the current knowledge of authigenic
220 carbonate precipitation in relation with the microbial processes related to sulfate reduction,
221 AOM and methanogenesis. Moreover, Torres et al. (2020) add complementary information on
222 the major role of silicate weathering for authigenic carbonate precipitation in anoxic
223 environments.

224 The $\delta^{13}C$ values of the authigenic dolomites associated with the gypsum veins from
225 the Neogene of Spain range between -11.9 and 7.3‰, and they thus display these typical
226 characteristics of ^{13}C-poor /^{13}C-rich methane-related carbonates. Moreover, as shown by
227 Chatterjee et al (2011), at the Sulfate Methane Transition Zone (SMTZ) where authigenic
228 dolomite precipitates, the upward flux of ^{13}C-rich DIC issued from the methanogenesis zone
229 modulates the relative contribution of ^{13}C-poor DIC derived from Anaerobic Oxidation of
230 Methane (AOM), thus supporting the large spatial and temporal variability of $\delta^{13}C$ values of
231 the authigenic dolomites in these environments.

232 The oxygen isotopic fractionation factor between dolomite and water depends on
233 temperature ($1000 \ln \alpha^{18}O$ dolomite-water $= 2.73 \times 10^6 T^{-2} + 0.26$; Vasconcelos et al., 2005).
234 This equation is used to estimate the temperature range of 15.6 to 40.3°C (Table 1) for the
235 authigenic dolomites that would have precipitated at equilibrium with seawater-derived fluids
236 characterized by $\delta^{18}O$ values ranging from 0.8 to 1.6‰, which are the values measured in the
237 present-day Western Mediterranean (Pierre, 1999). The estimated equilibrium temperatures of
238 dolomites differ in the studied basins: they are the lowest in Albox (15.6 to 24.4°C),
239 intermediate in Vera (19.6 to 28.5°C) and the highest in Murcia and Lorca (25.6 to 40.3°C).
240 Compared to the present-day Mediterranean bottom water temperature (~13°C), most of the
241 temperature estimations are much warmer, thus indicating that the diagenetic fluids were
242 issued from moderate to relatively great burial depths (up to 1 km for a normal geothermal
243 gradient).

244 4.1.2 Bacterial sulfate reduction

The production of hydrogen sulphide during bacterial sulfate reduction promotes the precipitation of sulfide minerals, generally as pyrite, which explains the close association of authigenic dolomite and pyrite that is observed in the dolomite nodules. During the sulfate reduction reaction, there is a large sulfur isotopic fractionation between the produced sulfide and the remaining sulfate that ranges from -46 to -77‰ in natural environments (Brunner and Bernasconi, 2005; Canfield et al., 2010; Meister et al., 2019; Rees, 1973; Rudnicki et al., 2001; Sim et al. 2011; Wortmann et al., 2001). As a result, if the initial source of dissolved sulfate is from seawater, the produced sulfide would have very negative $\delta^{34}S$ values whereas the residual sulfate would exhibit $\delta^{34}S$ values higher than the seawater source. The rate of the sulfate reduction reaction has a critical importance in controlling the ratio of the enrichment factors $\varepsilon^{34}S/\varepsilon^{18}O$ in the residual sulfate; it is generally close to 2.5 (Mizutani and Rafter, 1973) but it may reach 4 when the amount of remaining sulfate becomes very low (Böttcher et al., 1998; Brunner et al., 2005).

The $\delta^{34}S$ values of the gypsum veins from the Neogene marls of Spain are depleted by 10.5 to 43.3‰ relative to evaporitic gypsum precipitated from the Cenozoic seawater sulfate (Evans et al., 2015; Garcia-Veigas et al., 2019); they are thus clearly issued from sulfide that was produced by the bacterial reduction of the initial source of seawater sulfate. Sulfide was probably precipitated as pyrite both within the dolomite framework and in conduits and fractures where fluids circulated in the sediments.

4.2 The biogeochemical reactions under oxic conditions

Under oxic conditions, pyrite is rapidly oxidized as iron oxy-hydroxides and sulfuric acid that reacts with the carbonate and clay minerals of the sedimentary matrix to produce authigenic sulfate and silica minerals (Fig. 8). Gypsum is the most important product of this oxidation process and it may be associated with alunite and silica. The association of authigenic natroalunite, anhydrite and silica was previously discovered in the middle Miocene evaporites from the Gulf of Suez (Rouchy and Pierre, 1987). Authigenic gypsum was also described in active methane seeps of the West African margin and of the Sea of Marmara where it occurred as euhedral crystals disseminated in the organic-rich sediment in association with methane-derived authigenic carbonates (Crémière et al., 2012; Pierre, 2017).

The sulfur isotope fractionation during pyrite oxidation is close to zero (Nakai and Jensen, 1964; Mizutani and Rafter, 1969), so that the $\delta^{34}S$ values of gypsum are quite similar to those of the pyrite from which they are derived.

The oxidation of pyrite occurs either during early diagenesis with oxygen-rich seawater, or later when the deposits are uplifted and flushed by groundwaters and surficial meteoric waters. Because the oxidation of pyrite uses both oxygen of water and molecular dissolved oxygen to produce aqueous sulfate, the relative contribution of these two sources control the oxygen isotopic composition of sulfate. Van Everdingen and Krouse (1965) have defined the following equation that relies the different parameters of the reaction.

$$\delta^{18}O_{SO4\text{-}ox} = f\,(\delta^{18}O_{water} + \varepsilon_{water}) + (1\text{-}f)\,(\delta^{18}O_{O2} + \varepsilon_{O2})$$

The enrichment factors during this process (ε_{water} = 4.1‰, ε_{O2} = -11.2‰) were estimated by Lloyd (1967) and Mizutani and Rafter (1969), later revised by Taylor et al (1987). Most experiments have shown that water was the main source of oxygen during the oxidation of sulfide (about 66% for Taylor et al, 1987; from 85 to 92% for Balci et al, 2007). These results indicate that the value of f would range between 1 and ~0.7.

For the gypsum veins of SE Spain, the $\delta^{18}O$ values of water used during pyrite oxidation were estimated using the $\delta^{18}O$ value of molecular oxygen (23.5‰ VSMOW; Kroopnick and Craig, 1972) and the fraction f of oxygen of water that would range between 1 and 0.66. Moreover, it is necessary to consider the isotopic fractionation between the aqueous and solid sulfate ($\varepsilon^{18}O$ = 3.5‰, Lloyd, 1968; $\varepsilon^{34}S$ = 1.7‰, Thode and Monster, 1965), which is the case when gypsum precipitation occurs from gypsum-saturated solutions in open system conditions. These fractionation factors measured by Van Driessche et al. (2016) from gypsum precipitation experiments display significant variations above 20°C and at low salinities, but they are close to those proposed by Lloyd and Thode and Monster below 20°C both in low and high salinities. The results of these estimations are reported in Table 1 and Fig. 9. The $\delta^{18}O$ values of water assumed for pyrite oxidation range between -9.8 to -0.9 when oxygen is issued only from water, and from -19.1 to -5.6 when oxygen is issued both from water and dissolved oxygen. Such ^{18}O-depleted values are characteristic of meteoric waters. However only some of them would be compatible with the regional hydroclimatic context from SE Spain where the average present-day $\delta^{18}O$ values of the local meteoric waters vary in the range ~ -6.0‰ in Murcia to ~-4‰ in Almeria (Araguas-Araguas and Diaz Teijeiro, 2005).

Lower $\delta^{18}O$ values of meteoric waters would have been recorded during glacial times due the global decrease of temperatures. Using the Dansgaard equation (1964) for an average 5°C decrease of temperature during glacial times, the $\delta^{18}O$ values of meteoric waters can be estimated to have ranged from -10.5 to -8.5‰. Finally the few $\delta^{18}O$ values of water that are higher than the present-day meteoric waters but lower than the present-day seawater, could correspond to mixtures between these two water sources.

Overall, these results exclude any relationship of the gypsum veins with the Tortonian-Messinian evaporites. They also prove that the gypsum veins were not produced during early diagenetic pyrite oxidation with seawater, but they clearly indicate late diagenetic oxidation with waters of meteoric origin. The pyrite oxidation process was following the final tectonic uplift of the sedimentary deposits that occurred differently according to the different basins but was completed in the late Pliocene. These deposits were drained with groundwaters more or less oxygenated leading to the precipitation of the gypsum veins along circulation pathways of gypsum-saturated solutions.

5. Conclusion

Secondary gypsum veins in sedimentary deposits led often to questioning about their origin. They might be related to circulation of gypsum-saturated solutions issued from connate evaporitic brines, dissolution of sulfate evaporite deposits, or oxidation of sulfide ore deposits (Dogramaci et al., 2017). In the present study the oxygen and sulfur isotopic compositions of gypsum were used to characterize the source of sulfate and to replace the diagenetic processes in the sedimentary and tectonic context during the Neogene in SE Spain. The gypsum veins present in the Tortonian, Messinian and Pliocene marls are the ultimate products of the complex history of these basins during this period. This history was marked by the important restriction of the marine environment that caused the deposition of organic-rich sediments, with high sedimentation rates, leading further to intense methanogenesis, responsible of the formation of methane-derived dolomites associated with sulfide minerals (pyrite). The circulation of oxygenated groundwaters in the sedimentary series was responsible for the oxidation of pyrite that was precipitating gypsum in veins networks. This occurred in a first stage of the sea-level drawdown during the Messinian salinity crisis and later after the MSC due to the progressive uplift of the Betic cordillera.

336 Acknowledgments

337 The authors are grateful to Jérôme Demange for his assistance during isotope analysis in
338 LOCEAN, and to Omar Boudouma for the SEM facilities in ISTEP (SU, Paris).

339 The authors thank Michael Böttcher and two anonymous reviewers for their very helpful
340 comments and advices to improve the manuscript.

341 Conflict of interest

342 The authors declare that there is no conflict interest with third parties.

343

344 References

345 Aiello, I., Garrison, R.E., Moore, J.C., Kastner, M., Stakes, D.S., 2001. Anatomy and origin
346 of carbonate structures in a Miocene cold-seep field. Geology, 29, 12, 111-1114.

347 Alperin, M.J., Reeburgh, W.S., Whiticar, M.J., 1988. Carbon and hydrogen isotope
348 fractionation resulting from anaerobic methane oxidation. Global Biogeochem Cycles 2(3),
349 279–288.

350 Araguas-Araguas L.J., Diaz Teijeiro M.F., 2005. Isotope composition of precipitation and
351 water vapour in the Iberian Peninsula. In IAEA-Tecdoc-1453. Isotopic composition of
352 precipitation in the Mediterranean Basin in relation to air circulation patterns and climate.
353 Final report of a coordinated research project 2000-2004. 173-190.

354 Balci, N., Shanks III, W.C., Mayer, B., Mandernack, K.W., 2007. Oxygen and sulfur isotope
355 systematics of sulfate produced by bacterial and abiotic oxidation of pyrite. Geochim.
356 Cosmochim. Acta, 71: 3796-3811.

357 Boschetti, T., Iacumin, P., 2005. Continuous flow $\delta^{18}O$ measurements : new approach to
358 standardization, high temperature thermodynamic and sulfate analysis. Rapid Commun. Mass
359 Spectrom. 19 :3007-3013. http://dx.doi.org/10.1002/rcm.2161

360 Böttcher, M.E., Brumsack, H.J., de Lange, G.J., 1998. Sulfate reduction and related stable
361 isotope (^{34}S, ^{18}O) variations in interstitial waters of the eastern Mediterranean. In : Robertson,
362 A.H.F., Richter, C., Camerlenghi, A. (Eds.), Proc. ODP : Sci. Results, 160. Ocean Drilling
363 Program, College Station, TX. pp. 365-373.

364 Brunner, B., Bernasconi, S.M., 2005. A revised isotope fractionation model for dissimilatory
365 sulfate reduction in sulfate reducing bacteria. Geochim. Cosmochim. Acta 69 (20), 4759-4771.

366 Brunner, B., Bernasconi, S.M., Kleikemper, J., Schroth, M.H., 2005. A model for oxygen and
367 sulfur isotope fractionation in sulfate during bacterial sulfate reduction processes. Geochim.
368 Cosmochim. Acta 69 (20), 4773-4785.

369 Canfield, D.E., Farquhar, J., Zerkle, A.L., 2010. High isotope fractionations during sulfate
370 reduction in a low-sulfate euxinic ocean analog. Geology 38, 5, 415-418.

371 Caruso A., Blanc-Valleron, M.-M., Da Prato, S., Rouchy, J.M., 2020. The late Messinian
372 "Lago-Mare" event and the Zanclean Reflooding in the Mediterranean Sea: New insights
373 from the Cuevas del Almanzora section (Vera Basin, South-Eastern Spain. Earth-Science
374 Reviews, 200, 102993

375 Chatterjee, S., Dickens, G.R., Bhatnagar, G., Chapman, W.G., Dugan, B., Snyder, G.T.,
376 Hirasaki, G.J., 2011. Pore water sulfate, alkalinity, and carbon isotope profiles in shallow
377 sediment above marine gas hydrate systems : A numerical modeling perspective. J.G.R., 116,
378 B09103, doi :10.1029/2011JB008290.

379 Claypool, G.E., Threlkeld, C.N., 1983. Anoxic diagenesis and methane generation in
380 sediments of the Blake Outer Ridge. Deep Sea Drilling Project Site 533, Leg 76. In : Sheridan,
381 R.E., Gradstein, F.M., et al. (Eds.), Init. Repts. DSDP, 76, U.S. Govt. Printing Office,
382 Washington, pp. 391-402.

383 Corbí, H., Soria, J.M., Lancis, C., Giannetti, A., Tent-Manclús, J.E., Dinarès-Turell, J., 2016.
384 Sedimentological and paleoenvironmental scenario before, during, and after the Messinian
385 Salinity Crisis: The San Miguel de Salinas composite section (western Mediterranean). Mar.
386 Geol., 379, 246–266.

387 Craig, H., 1957. Isotopic standards for carbon and oxygen and correction factors for mass-
388 spectrometric analysis of carbon dioxide. Geochim. Cosmochim. Acta, 12,133–149.

389 Crémière, A., Pierre, C., Blanc-Valleron, M.M., Zitter, T., Cagatay, N.M., Henry, P., 2012.
390 Methane-derived authigenic carbonates along the North Anatolian fault system in the Sea of
391 Marmara (Turkey). Deep Sea Res., I, 66, 114-130.

392 Dansgaard, W., 1964. Stable isotopes in precipitation. Tellus, 4, 438-467.

De Larouzière, F.D., Bolze J., Bordet, P., Hernandez, J., Montenat, C., Ott d'Estevou, P., 1988. The Betic segment of the lithospheric Trans-Alboran shear zone during the Late Miocene. Tectonophysics, 152, 41–52.

Dela Pierre, F., Martire, L., Natalicchio, M., Clari, P., Petrea, C., 2010. Authigenic carbonates in Upper Miocene sediments of the Tertiary Piedmont Basin (NW Italy) : Vestiges of an ancient gas hydrate stability zone ? GSA Bull., 122, 7/8, 994-1010.

Dogramaci, S., Mc Lean, L., Skrzypek, G., 2017. Hydrochemical and stable isotope indicators of pyrite oxidaton in carbonate-rich environment ; the Hamersley Basin, Western Australia. Journal of Hydrology, 545, 288-298.

Gonfiantini, R., Stichler, W., Kozanski, K., 1995. Standards and intercomparison materials distributed by the International Atomic Energy Agency for stable isotope measurements. In: Reference and Intercomparison Materials for Stable Isotopes of Light Elements, IAEA-TECDOC-825. IAEA, Vienna, pp 13–29.

Evans, N., Turchyn, A., Gazquez, F., Bontognali, T.R.R., Chapman, H.J., Hodell, D.A., 2015. Coupled measurements of $\delta^{18}O$ and δD of hydration water and salinity of fluid inclusions in gypsum from the Messinian Yesares Member, Sorbas Basin (SE Spain). Earth Planet. Sci. Lett., 430, 499-510.

Garcia-Veigas, J., Gibert, L., Cendon, D.I., Artiaga, D., Corbi, H., Soria, J.M., Lowenstein, T.K., Sanz, E., 2019. Late Miocene evaporite geochemistry of Lorca and Fortuna basins (Eastern Betics, SE Spain). Evidence of restriction and continentalization. Basin Research. Doi :10.1111/bre.12408

Guerra-Merchán, A., Serrano, F., 1993. Tectonosedimentary setting and chronostratigraphy of the Neogene reefs in the Almanzora corridor (Betic Cordillera, Spain). Geobios, 26, 57-67.

Halas, S., Szaran, J., 2001. Improved thermal decomposition of sulfates to SO_2 and mass spectrometric determination of $\delta^{34}S$ of IAEA SO-5, IAEA SO-6 and NBS-127 sulfate standards. Rapid Commun. Mass Spectrom., 15, 1618-1620.

Hoareau, G., Odonne, F., Debroas, E.J., Maillard, A., Monnin, C., Callot, P., 2009. Dolomitic concretions in the Eocene Sobrarbe delta (Spanish Pyrenees): Fluid circulation above a submarine slide scar infilling. Mar. Petrol. Geol., 26, 724-737.

Konhauser, K., 2007. Introduction to geomicrobiology, Blackwell Publishing, UK, pp.84-89.

Krijgsman, W., Leewis, M.E., Garcés, M., Kouwenhoven, T.J., Kuiper, K.F., Sierro, F.J., 2006. Tectonic control for evaporite formation in the Eastern Betics (Tortonian; Spain). Sediment. Geol. 188–189, 155–170.

Kroopnick, P., Craig, H., 1972. Atmospheric Oxygen: Isotopic Composition and Solubility Fractionation. Science 175 (4017), 54-55.

Lloyd, R.M., 1967. Oxygen 18 composition of oceanic sulfate. Science, 156, 1228-1231.

Lloyd, R.M., 1968. Oxygen isotope behavior in the sulfate-water system. J. G. Res., 73 (18), 6099-6110.

Longinelli, A., Craig, H., 1967. Oxygen 18 variations in sulfate ions in sea-water and saline lakes. Science, 156, 56-59.

Meijninger, B.M.L., Vissers, R.M.L., 2006. Miocene extensional basin development in the Betic Cordillera, SE Spain, revealed through analysis of the Alhama de Murcia and Crevillente Faults. Basin Research, 18, 547-571. doi: 10.1111/j. 1365-2117.2006.00308.x.

Meister, P., Reyes, C., 2019. The carbon isotope record of the sub-seafloor biosphere. Geosciences, 9, 507, 1-25.

Meister, P., Brunner, B., Picard, A., Böttcher, M.E., Jørgensen, B.B., 2019. Sulphur and carbon isotopes of past sub-seafloor microbial activity. Nature Scientific Reports, 9, 604, 1-9.

Mizutani, Y., Rafter, T.A., 1973. Isotopic behaviour of sulphate oxygen in the bacterial reduction of sulphate. Geochem. J., 6, 183-191.

Montenat, C., Bizon, G., 1976. A propos de l'évolution géodynamique Mio-Pliocène en Méditerranée occidentale. L'exemple du bassin de Vera (Cordillères bétiques, Espagne méridionale). C.R. Som. Soc. Géol. Fr., 1, 15-16.

Montenat, C., 1977. Les bassins néogènes du Levant d'Alicante et de Murcia (Cordillères bétiques orientales, Espagne). Stratigraphie, paléogéographie et évolution dynamique. Doc. Lab. Géol. Fac. Sci. Lyon, 69, 345 pp.

Montenat, C., Ott d'Estevou, Ph., Masse, P., 1987. Tectonic–sedimentary characters of the

449 Betic Neogene basins evolving in a crustal transcurrent shear zone (SE Spain). Bull. Cent.
450 Rech. Explor.-Prod. Elf-Aquitaine, 11, 1–22.

451 Montenat, C., Ott d'Estevou, P., Aellen de la Chapelle, M. (1990). Les séries Néogènes entre
452 Lorca et Huercal Overa. Documents et Travaux de l'Institut Géologique Albert de Lapparent
453 (IGAL), 12-13, 281-286.

454 Nakai, N., Jensen, M.L., 1964. The kinetic isotope effect in the bacterial reduction and
455 oxidation of sulfur. Geochim. Cosmochim. Acta, 28, 1893-1912.

456 Nyman, S.L., Nelson, C.S., Campbell, K.A., 2010. Miocene tubular concretions in East Coast
457 Basin, New Zealand : Analogue for the subsurface plumbing of cold seeps. Mar. Geol., 272,
458 319-336.

459 Oppo, D., Viola, I., Capozzi, R., 2017. Fluid sources and stable isotope signatures in
460 authigenic carbonates from the Northern Apennines, Italy. Mar. Petrol. Geol., 86, 606-619.

461 Pedrera, A., Galindo-Zaldívar, J., Tello, A., Marín-Lechado, C., 2010. Intramontane basin
462 development related to contractional and extensional structure interaction at the termination of
463 a major sinistral fault: the Húercal-Overa Basin (Eastern Betic Cordillera). J. Geodynamics,
464 49, 5, 271-286. Doi :10.1016/j.jog.2010.01.008. hal-00618180

465 Pierre, C., 1999. The oxygen and carbon isotope distribution in the Mediterranean water
466 masses. Mar. Geol., 153, 41-55.

467 Pierre, C., 2017. Origin of the authigenic gypsum and pyrite from active methane seeps of the
468 southwest African margin. Chem. Geol. 449, 158-164.

469 Pierre, C., Caruso, A., Blanc-Valleron, M.-M., Rouchy, J.M., Orzsag-Sperber, F., 2006.
470 Reconstruction of the paleoenvironmental changes around the Miocene–Pliocene boundary
471 along a West–East transect across the Mediterranean. Sediment. Geol., 188–189 319–340.

472 Pierre C., Rouchy J.M., 2004. Isotopic composition of diagenetic dolomites in the Tortonian
473 marls of the Western Mediterranean margins : evidence of past gas hydrate formation and
474 dissociation. Chem. Geol., 205, 469-484

475 Pierre, C., Rouchy, J.M., Blanc-Valleron, M.M., 2002. Gas hydrates dissociation in the Lorca
476 Basin (SE Spain) during the Messinian salinity crisis. Sediment. Geol., 147, 247-252

Pierre, C., Rouchy, J.M., Blanc-Valleron, M.M., 2018. Carbonate diagenesis related to methane-rich fluid migration on continental margins : examples of the dolomite concretions in the Neogene marls of South-East Spain. AGU fall meeting, Washington, 10-14 December 2018

Pierre, C., Rouchy, J.M., Blanc-Valleron, M.M., Etoubleau, J., Fouquet, Y., 2015. Methanogenesis and clay minerals diagenesis during the formation of dolomite nodules from the Tortonian marls of southern Spain. Mar. Petrol. Geol., 66, 606-615.

Rees, C.E., 1973. A steady-state model for sulphur isotope fractionation in bacterial reduction processes. Geochim. Cosmochim. Acta, 37, 1141-1162.

Rosenbaum, J., Shepard, S.M.F., 1986. An isotopic study of siderites, dolomites and ankerites at high temperatures. Geochim. Cosmochim. Acta, 50, 1147-1150.

Rouchy, J.M., Pierre, C., 1987. Authigenic natroalunite in middle Miocene evaporites from the Gulf of Suez (Gemsa, Egypt). Sedimentology, 34, 807-812.

Rouchy, J.M., Bernet-Rolande, M.C., Maurin, A.F., 1994. Descriptive petrography of evaporites : applications in the field, subsurface and the laboratory. In : Evaporite sequences in petroleum exploration. 1. Geological methods. Editions Technip (ISBN (vol. 1) 2-7108-0624X, 70-135.

Rouchy, J.M., Taberner, C., Blanc-Valleron, M.-M., Sprovieri, R., Russell, M., Pierre, C., Stefano, E.D., Pueyo, J.J., Caruso, A., Dinares-Turell, J., Gomis-Coll, E., Wolff, G.A., Cespuglio, G., Ditchfield, P., Pestrea, S., Combourieu-Nebout, N., Santisteban, C., Grimalt, J.O., 1998. Sedimentary and diagenetic markers of the restriction in a marine basin: the Lorca Basin (SE Spain) during the Messinian. Sediment. Geol., 121, 23–55.

Rudnicki, M.D., Elderfield, H., Spiro, B., 2001. Fractionation of sulfur isotopes during bacterial sulfate reduction in deep ocean sediments at elevated temperatures. Geochim. Cosmochim. Acta, 65 (5), 777-789.

Sanz de Galdeano, C., 1990, Geologic evolution of the Betic Cordilleras in the Western Mediterranean, Miocene to the present. Tectonophysics, 172, 107–119, https://doi .org/10.1016/0040-1951(90)90062-D.

Sanz de Galdeano, C., Vera, J.A., 1992. Stratigraphic record and palaeogeographical context

of the Neogene basins in the Betic Cordillera, Spain. Basin Res., 4, 21–36.

Sim, M.S., Ono, S., Donovan, K., Templer, S.P., Bosak, T., 2011. Effect of electron donors on the fractionation of sulfur isotopes by a marine *Desulfovibrio* sp. Geochim. Cosmochim. Acta, 75, 4244-4259.

Taylor, B.E., Wheeler, M.C., Nordstrom, D.K., 1987. Isotope composition of sulfate in acid mine drainage as measures of bacterial oxidation. Nature, 308, 530-541.

Thode, H.G., Monster, J., 1965. Sulfur isotope geochemistry of petroleum, evaporites and ancient seas. In : Fluids in Subsurface Environments. A.A.P.G. Memoir 4, pp. 367-377.

Torres, M., Hong, W.L., Solomon, E.A., Milliken, K., Kim, J.H., Sample, J.A., Teichert, B.M.A., Wallmann, K., 2020. Silicate weathering in anoxic marine sediment as a requirement for authigenic carbonate burial. Earth-Sci. Rev., 200, 102960.

Van Driessche, A.E.S., Canals, A., Ossorio, M., Reyes, R.C., Garcia-Ruiz, J.M., 2016. Unravelling the sulfate sources of (giant) gypsum crystals using gypsum isotope fractionation factors. J. Geol., 124, 235-245.

Van Everdingen, R.O., Krouse, H.R., 1965. Isotope composition of sulphates generated by bacterial and abiological oxidation. Nature, 315, 395-396.

Vasconcelos, C., Mc Kenzie, J.A., Warthmann, R., Bernasconi, S.M., 2005. Calibration of the $\delta^{18}O$ paleothermometer for dolomite precipitated in microbial cultures and natural environments. Geology, 33, 4, 317-320.

Whiticar, M.J., 1999. Carbon and hydrogen isotope systematics of bacterial formation and oxidation of methane. Chem. Geol., 161:291–314.

Whiticar, M.J., Faber, E., 1986. Methane oxidation in sediments and water column environments-isotopic evidence. Org. Geochem., 10, 759-768.

Wortmann, U.G., Bernasconi, S.M., Böttcher, M.E., 2001. Hypersulfidic deep biosphere indicates extreme sulfur isotope fractionation during single-step microbial sulfate reduction. Geology, 29 (7), 647-650.

Figure captions

Figure 1 : Schematic geological map of the SE Spain. Location of the sampling sites.

Figure 2 : Field views of the dolomite nodules and gypsum veins from the Neogene marls of SE Spain. A : Dense network of gypsum veins crossing the lower Pliocene deposits in the Vera Basin. B : dolomite nodule with internal veins of microcrystalline gypsum , Vera Basin ; C : Dolomite nodule surrounded by fibrous gypsum layer, Vera Basin. D : Group of dolomite nodules surrounded by fibrous gypsum layer and within marls crossed by gypsum veins, Albox Basin. E : mega-nodules of dolomite crossed by veins of fibrous gypsum with aggregates of and large selenitic crystals filling a central cavity (arrow), Murcia Basin. F : View of the lower part of the diatomite-bearing unit composed of alternating diatomites, siltstones, and dolomitic carbonate layers with gypsum veins (arrows), and containing alunite nodules, Lorca Basin.

Figure 3 : Simplified lithological successions of the Neogene basins of Murcia, Vera, Albox and Lorca in SE Spain where the studied samples have been collected.

Figure 4 : Scanning Electron Microscope observations of the microfacies of the gypsum veins from the Neogene marls of SE Spain. A - Sample ES16-127 (Murcia Basin) : Fibrous layers of gypsum with various sedimentary particles cemented and intercalated between the gypsum layers. B - Sample ES16-36 (Vera Basin) : Palisadic layers of gypsum with intercalations of layers of sedimentary particles. C - Sample ES16-22 (Vera Basin) : Group of pyrite (now oxidized) framboids enveloped by silicate particles. D - Sample ES16-36 (Vera Basin): Inclusion of sediment with pyrite (now oxidized) framboids and octahedrons cemented by gypsum. E - Sample ES16-36 (Vera Basin): close-up of a group of pyrite octahedrons. F - Sample ES16-63 (Albox Basin): Pyrite (now oxidized) framboids and calcite crystals with numerous holes of dissolution.

Figure 5 : Oxygen and sulfur isotope composition of the gypsum veins from the Neogene marls of SE Spain. The range of the δ values of Tortonian-Messinian evaporitic gypsum from the Lorca, Sorbas and Fortuna basins (Evans et al., 2015; Garcia-Veigas et al., 2019).

Figure 6 : Scanning Electron Microscope observations of the microfacies of the dolomite nodules associated with the gypsum veins. A - Sample ES17-58 (Murcia Basin): Group of framboids of pyrite (mostly preserved) within the microcrystalline dolomite matrix containing large silicate particles. B - Sample ES16-13 (Vera Basin): Dolomite rhombs with numerous dissolution holes; small isolated pyrite crystals and one framboid are disseminated within the

565 matrix. C - Sample ES16-58 (Albox Basin): Group of framboids and isolated crystals of
566 pyrite (mostly preserved) within the microcristalline dolomite matrix. D - Sample ES-
567 62 (Albox Basin): Microcrystalline dolomite matrix containing numerous silicate particles
568 and crossed by a vein filled with framboids of pyrite (now mostly oxidized).

569 Figure 7 : Oxygen and carbon isotope composition of the dolomite of the nodules associated
570 with the gypsum veins from the Neogene marls of SE Spain.

571 Figure 8 : Sequence of the biogeochemical reactions leading to the diagenetic minerals
572 formation.

573 Figure 9 : Estimation of the $\delta^{18}O$ value of the water of oxidation of pyrite deduced from the
574 $\delta^{18}O$ value of gypsum. The calculation assumes gypsum precipitation in open system
575 conditions, and pyrite oxidation with only water oxygen (f = 1) and with water oxygen (f =
576 0.66) and molecular oxygen. The ranges of $\delta^{18}O$ values of local meteoric waters from SE
577 Spain are indicated for the present-day and extrapolated for glacial periods. The present-day
578 range of $\delta^{18}O$ values of the West Mediterranean seawater is also given for information.

579

580 Table caption

581 Table 1 : Short description and location of the gypsum veins close to the dolomite nodules
582 sampled in the Vera, Albox, Murcia and Lorca Basins. The $\delta^{18}O$ and $\delta^{13}C$ values of dolomite
583 and $\delta^{18}O$ and $\delta^{34}S$ values of gypsum are reported in this table. The equilibrium temperatures
584 of dolomite have been estimated for two $\delta^{18}O$ values of seawater (0.8 and 1.6‰). The $\delta^{18}O$
585 values of the water assumed for pyrite oxidation are estimated for open system conditions
586 with two values of the fraction f of water (1 and 0.66).

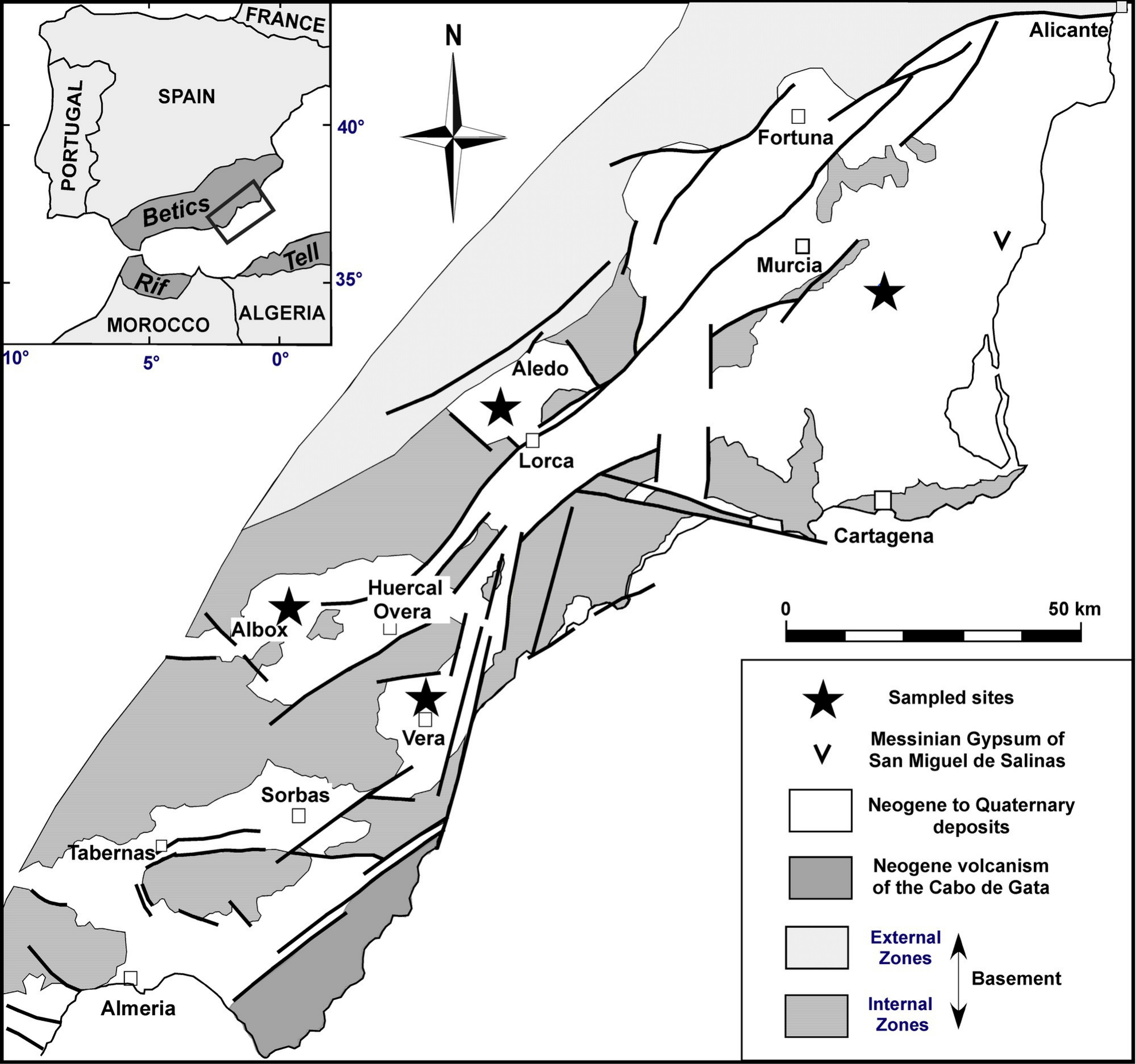
FRANCE
SPAIN
PORTUGAL
Betics
Rif
Tell
MOROCCO
ALGERIA
40°
35°
10°
5°
0°
N
Alicante
Fortuna
Murcia
Aledo
Lorca
Cartagena
Huercal
Overa
Albox
Vera
Sorbas
Tabernas
Almeria
0
50 km
Sampled sites
Messinian Gypsum of San Miguel de Salinas
Neogene to Quaternary deposits
Neogene volcanism of the Cabo de Gata
External Zones
Internal Zones
Basement


A


B


C


D


E


F

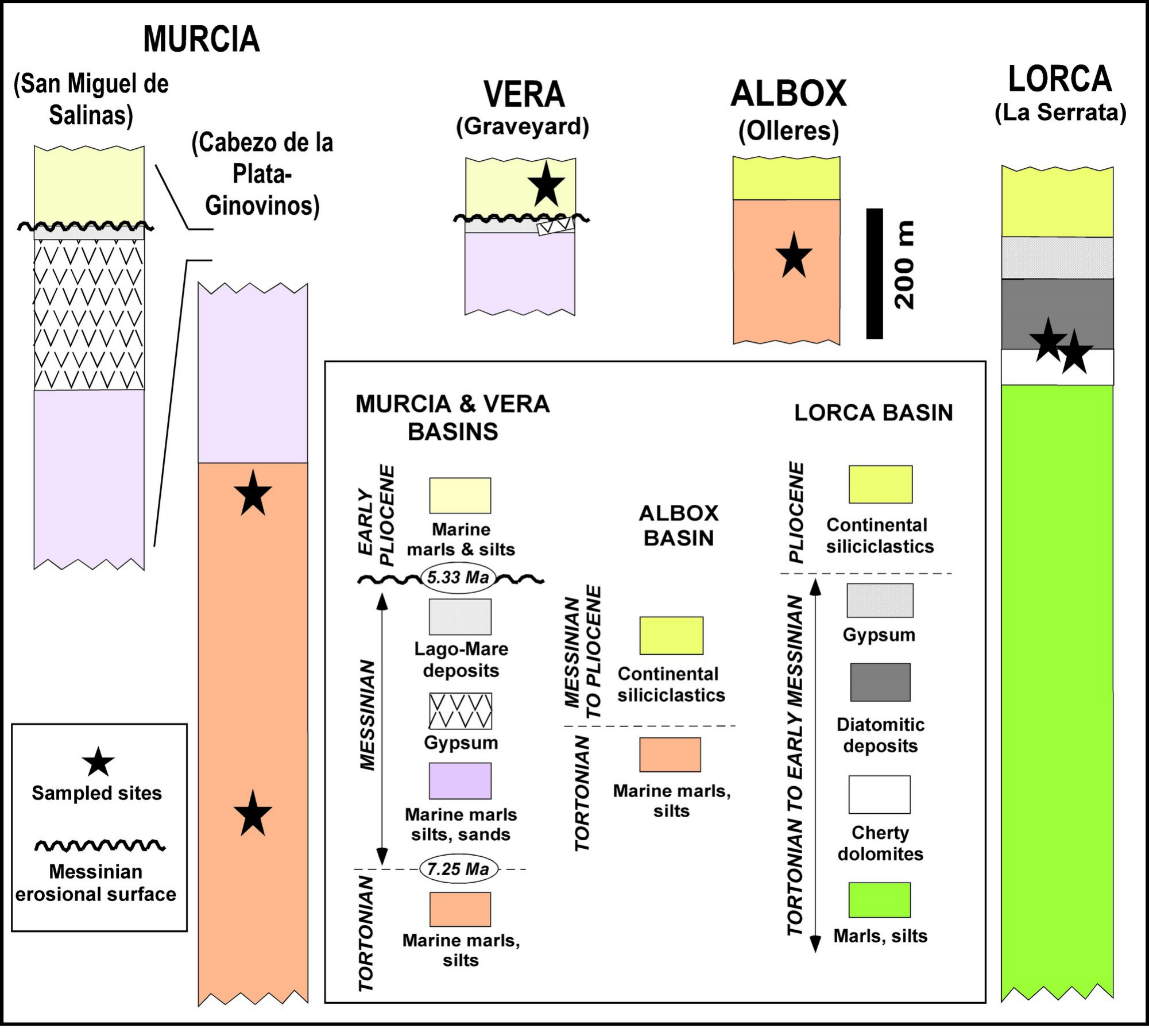
MURCIA
(San Miguel de Salinas)
(Cabezo de la Plata-Ginovinos)
VERA
(Graveyard)
ALBOX
(Olleres)
LORCA
(La Serrata)
200 m
Sampled sites
Messinian erosional surface
MURCIA & VERA BASINS
EARLY PLIOCENE
Marine marls & silts
5.33 Ma
MESSINIAN
Lago-Mare deposits
Gypsum
Marine marls silts, sands
7.25 Ma
TORTONIAN
Marine marls, silts
ALBOX BASIN
MESSINIAN TO PLIOCENE
Continental siliciclastics
TORTONIAN
Marine marls, silts
LORCA BASIN
PLIOCENE
Continental siliciclastics
TORTONIAN TO EARLY MESSINIAN
Gypsum
Diatomitic deposits
Cherty dolomites
Marls, silts

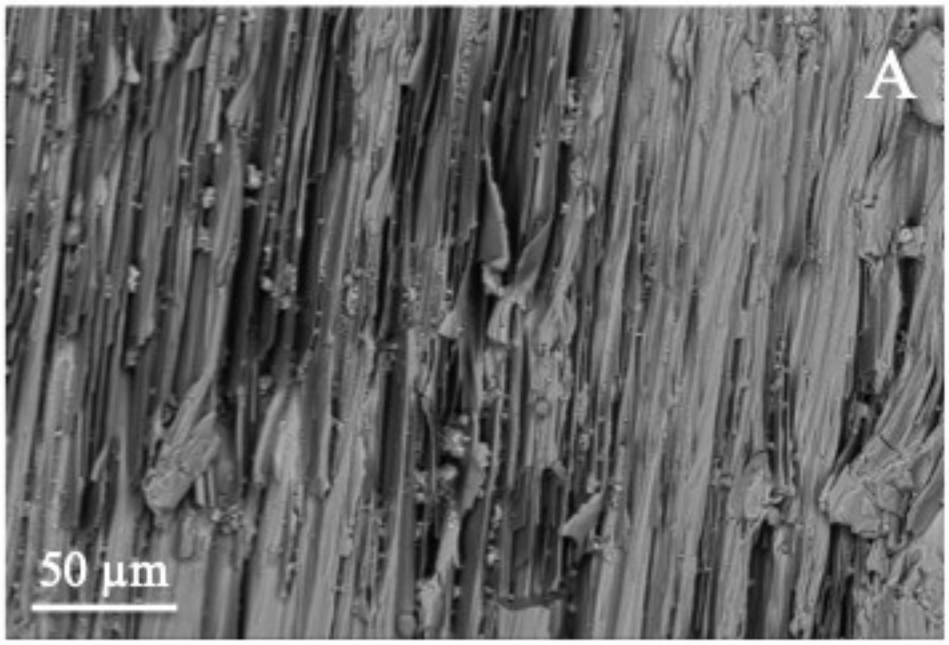
A
50 µm

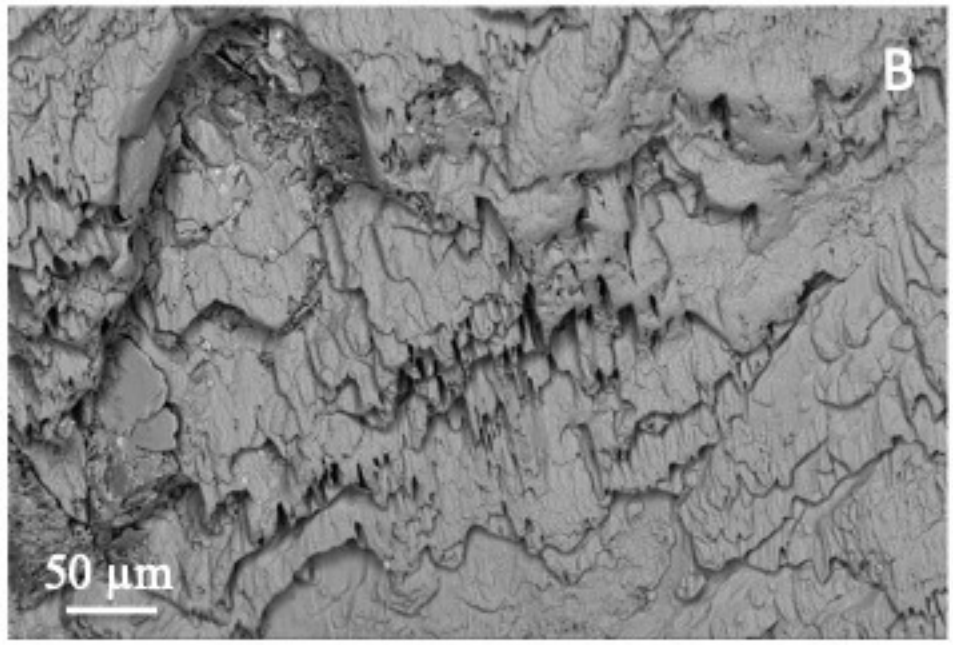
B
50 µm

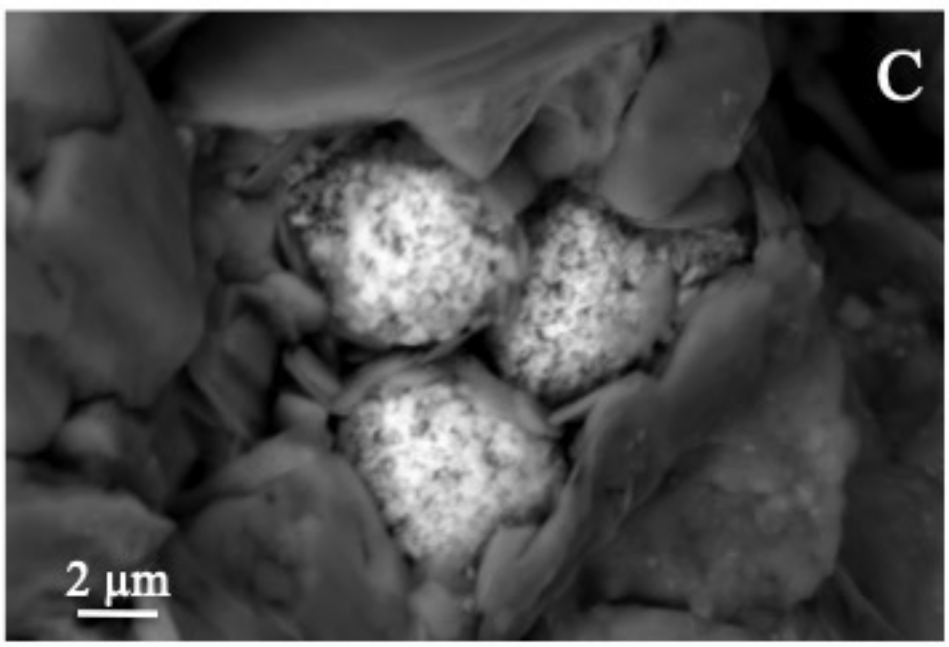
C
2 µm

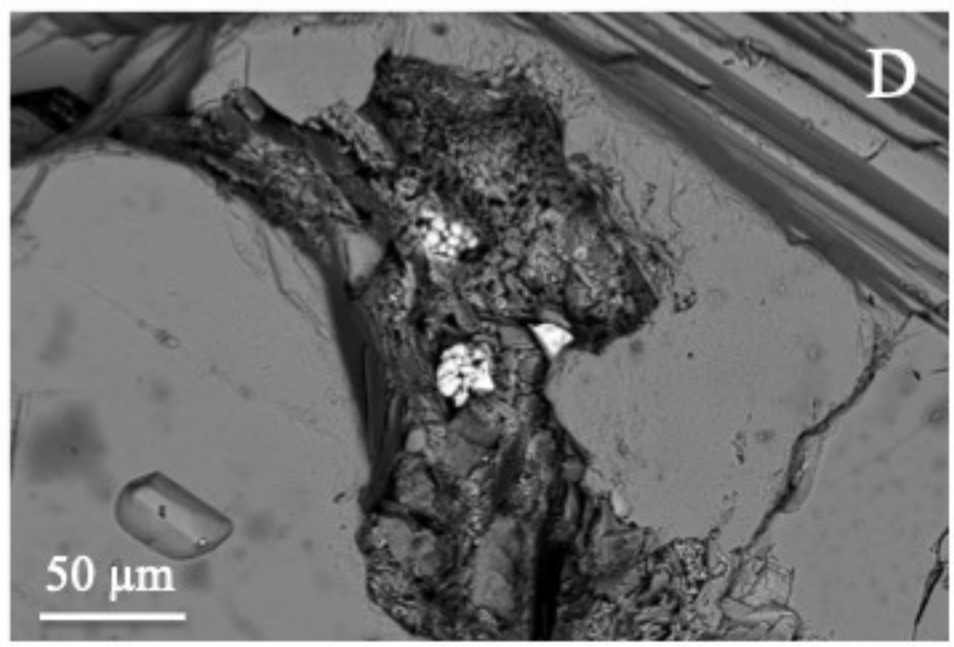
D
50 µm

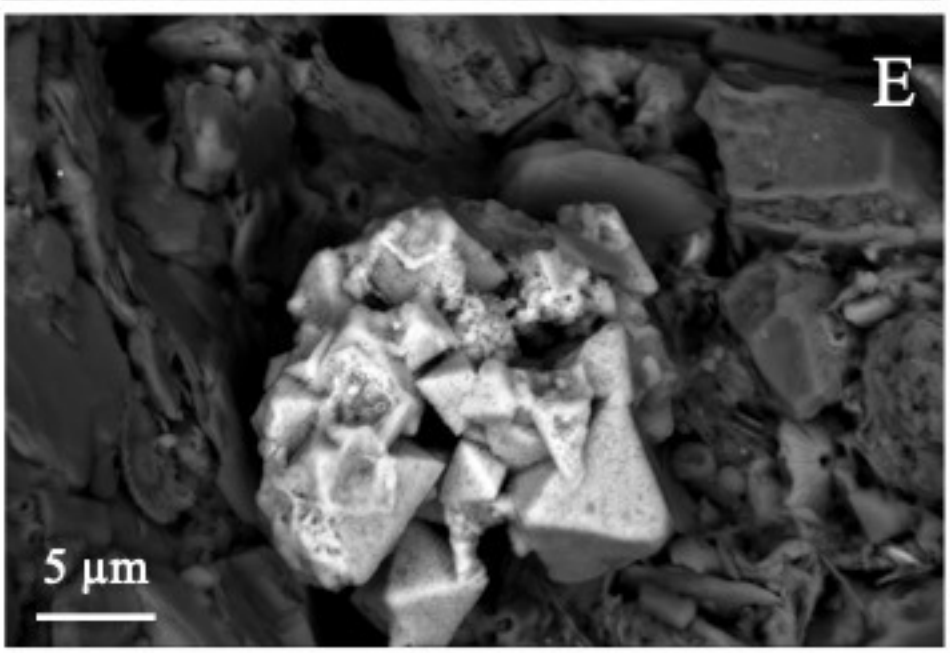
E
5 µm

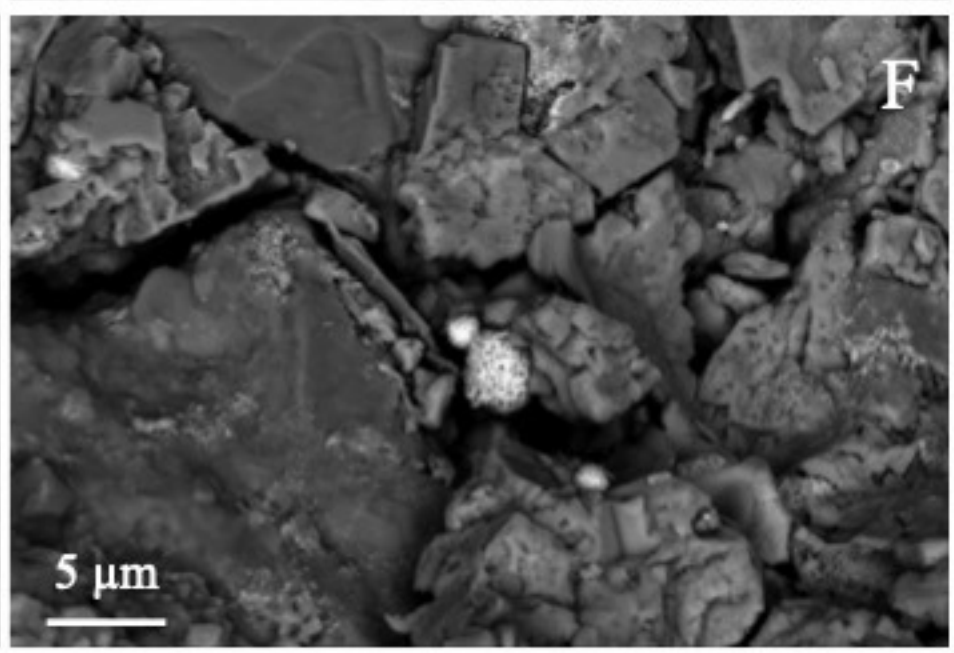
F
5 µm

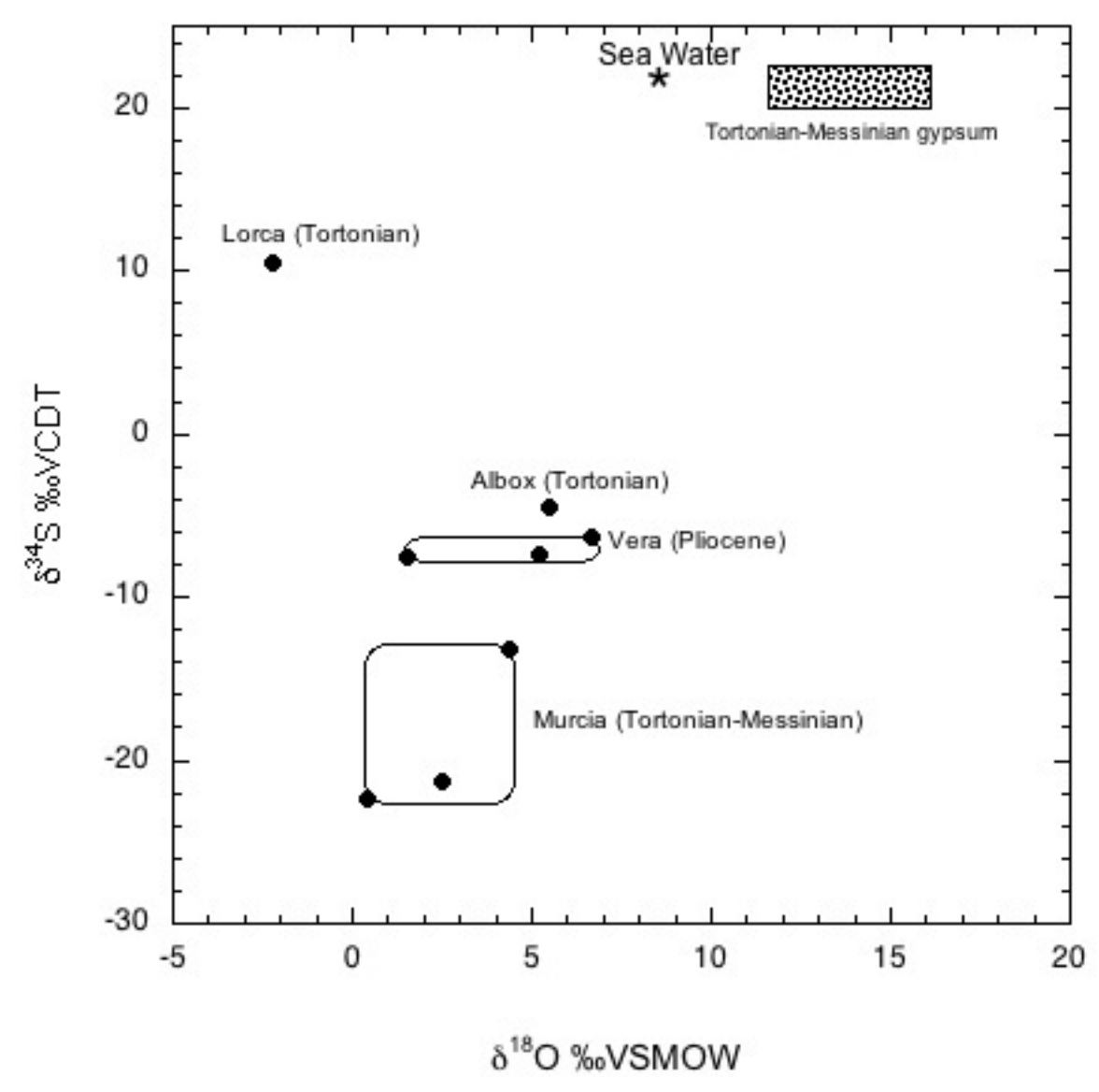
Sea Water
Tortonian-Messinian gypsum
Lorca (Tortonian)
Albox (Tortonian)
Vera (Pliocene)
Murcia (Tortonian-Messinian)
20
10
0
-10
-20
-30
-5
0
5
10
15
20
δ34S ‰VCDT
δ18O ‰VSMOW

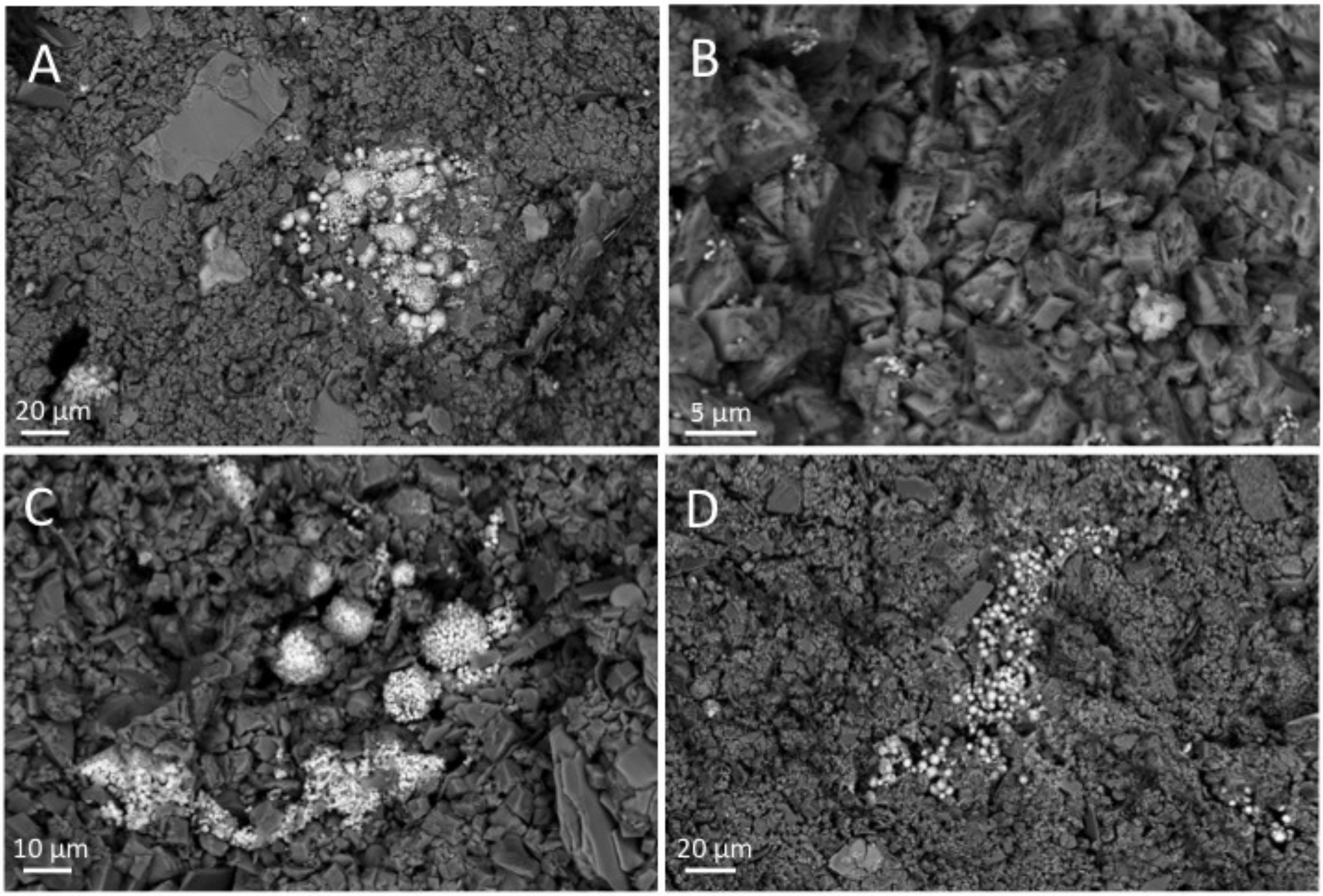
A
20 µm
B
5 µm
C
10 µm
D
20 µm

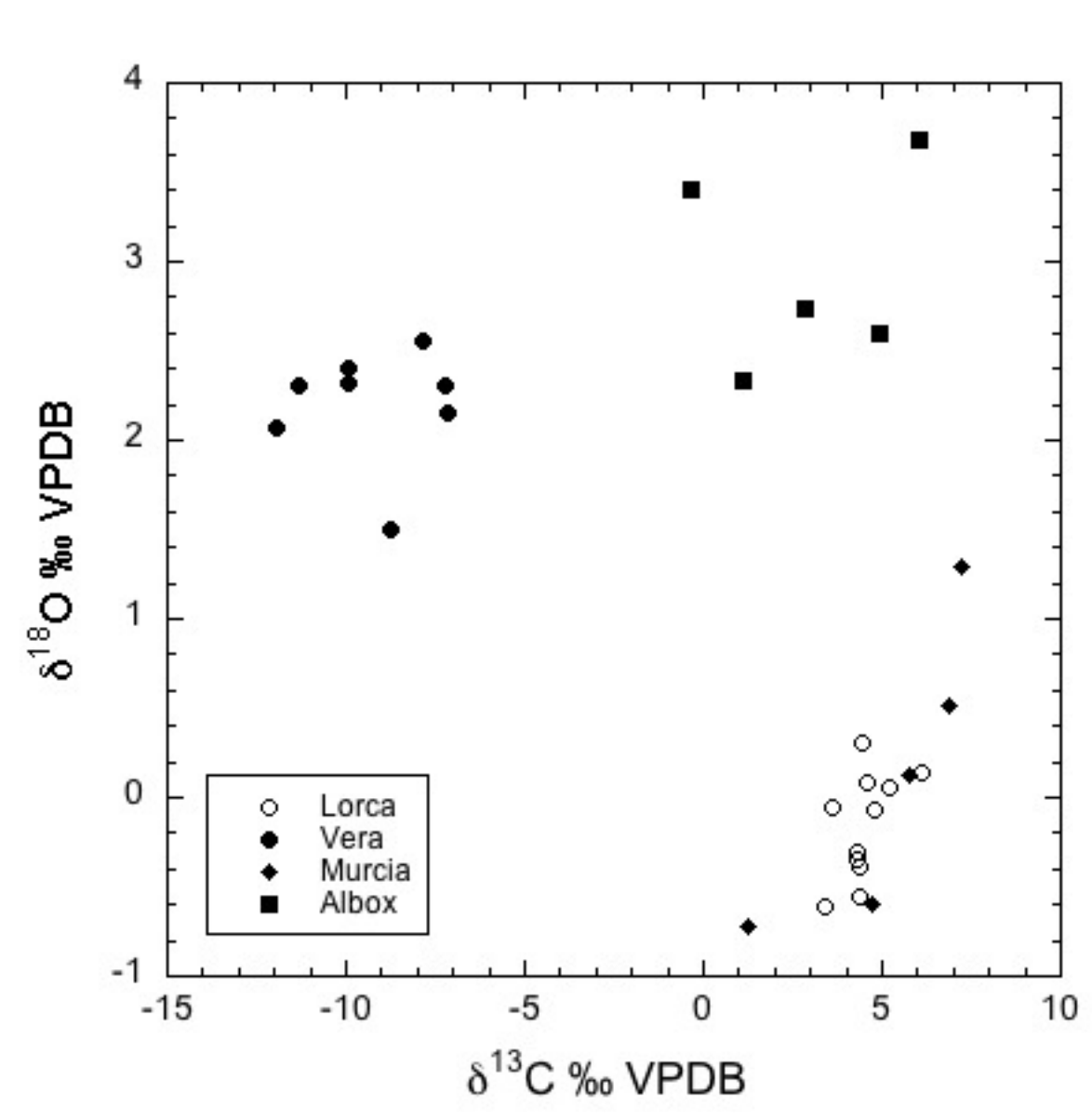
4
3
2
1
0
-1
-15
-10
-5
0
5
10
δ18O ‰ VPDB
δ13C ‰ VPDB
Lorca
Vera
Murcia
Albox

1) Bacterial reduction of sulfate coupled to Anaerobic Oxidation of Methane (AOM)

$CH_4 + SO_4^{2-} \rightarrow HS^- + HCO_3^- + H_2O$

2) Methanogenesis

$CH_3COO^- + H^+ \rightarrow CH_4 + CO_2$

3) Methanogenesis - CO_2 reduction

$CO_2 + 4H_2 \rightarrow CH_4 + 2\ H_2O$

4) Silicate weathering (with CO_2 produced during methanogenesis)

silicates + CO_2 $\rightarrow$ clays + cations + silica + HCO_3^-

5) Oxidation of pyrite : sulfuric acid production

$FeS_2 + 2O_2 + 2H_2O \rightarrow 2\ H_2SO_4$ + Fe-oxy-hydroxides

6a) Sulfuric acid weathering of carbonates : diagenetic gypsum formation

$CaCO_3 + 2H_2SO_4 + H_2O \rightarrow CaSO_4, 2(H_2O) + CO_2 + H_2O$

6b) Sulfuric acid weathering of clay minerals : diagenetic alunite and silica formation

illite + $2H_2SO_4$ $\rightarrow$ $3\ SiO_2 + KAl_3(SO_4)_2(OH)_6$

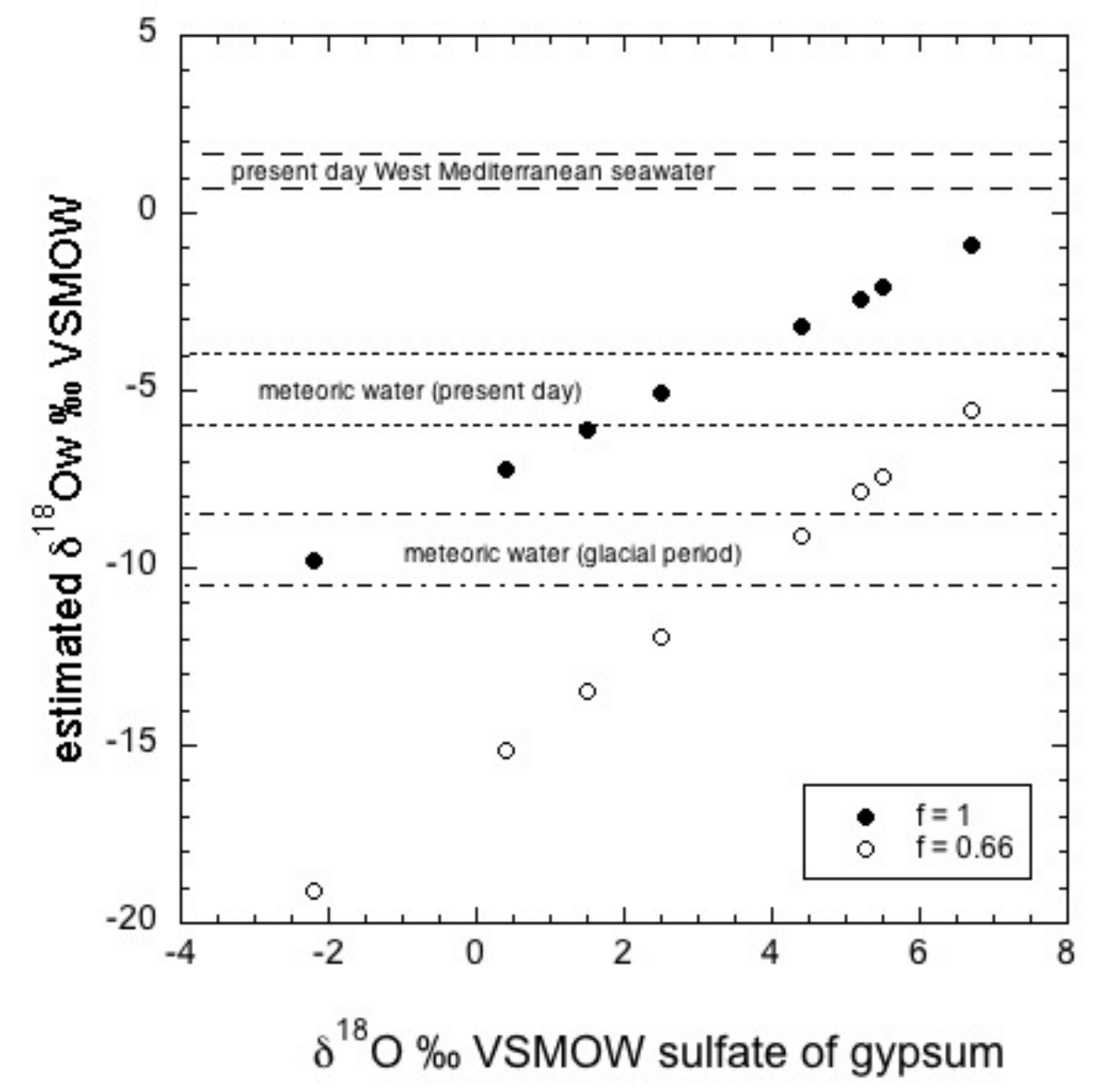
present day West Mediterranean seawater
meteoric water (present day)
meteoric water (glacial period)
f = 1
f = 0.66
estimated δ18Ow ‰ VSMOW
δ18O ‰ VSMOW sulfate of gypsum
5
0
-5
-10
-15
-20
-4
-2
0
2
4
6
8

Sample	Age	Basin	Section	Description	$\delta^{18}O$ ‰ VPDB dolomite	$\delta^{13}C$ ‰ VPDB dolomite	Equilibrium temperature °C $\delta^{18}O$ w =1.6‰	Equilibrium temperature °C $\delta^{18}O$ w = 0.8‰	$\delta^{34}S$ ‰ VCDT gypsum	$\delta^{18}O$ ‰ VSMOW gypsum	estimated $\delta^{18}Ow$ with f=1	estimated $\delta^{18}Ow$ with f=0.66
ES 16.16	Pliocene	Vera	graveyard	Nodule 1-external envelope	1.06	-7.01	30.5	26.5				
ES 16.17	Pliocene	Vera	graveyard	Nodule 1-internal part	1.73	-7.15	27.3	23.5				
ES 16.18	Pliocene	Vera	graveyard	Nodule 1-marly intercalation	1.5	-8.77	28.5	24.6				
ES 16.19	Pliocene	Vera	graveyard	Nodule 1-internal part	2,15	-7,12	25.3	21.5				
ES 16.20	Pliocene	Vera	graveyard	Nodule 1-lower internal part	2.56	-7.81	23.3	19.6				
ES 16.22	Pliocene	Vera	graveyard	Gypsum veins around nodule 1					-7.6	1.5	-6.1	-13.5
ES 16.30	Pliocene	Vera	graveyard	Group of nodules-core of nodule a	2.31	-11.29	24.5	20.7				
ES 16.31	Pliocene	Vera	graveyard	Group of nodules-core of nodule b	2.32	-9.94	24.5	20.7				
ES 16.32	Pliocene	Vera	graveyard	Group of nodules-core of nodule c	2.30	-7.20	24.5	20.7				
ES 16.33	Pliocene	Vera	graveyard	Group of nodules-core of nodule d	2.41	-9.92	24.0	20.3				
ES 16.34	Pliocene	Vera	graveyard	Group of nodules-core of nodule e	2.07	-11.93	25.7	21.9				
ES 16.36	Pliocene	Vera	graveyard	Gypsum veins					-7.4	5.2	-2.4	-7.8
ES 16.37	Pliocene	Vera	graveyard	Conduit with gypsum veins					-6.5	6.7	-0.9	-5.6
ES 16.57	Tortonien	Albox	between Albox and Saliente	Group of nodules-core of nodule 1	2.34	1.11	24.4	20.6				
ES 16.58	Tortonien	Albox	between Albox and Saliente	Group of nodules-core of nodule 2	3.41	-0.32	19.4	15.8				
ES 16.59	Tortonien	Albox	between Albox and Saliente	Group of nodules-core of nodule 3	2.73	2.85	22.5	18.8				
ES 16.61	Tortonien	Albox	between Albox and Saliente	Group of nodules-core of nodule 4	3.68	6.07	18.1	14.6				

Sample	Age	Basin	Section	Description	$\delta^{18}O$ ‰ VPDB dolomite	$\delta^{13}C$ ‰ VPDB dolomite	Equilibrium temperature °C $\delta^{18}O$ w =1.6‰	Equilibrium temperature °C $\delta^{18}O$ w = 0.8‰	$\delta^{34}S$ ‰ VCDT gypsum	$\delta^{18}O$ ‰ VSMOW gypsum	estimated $\delta^{18}Ow$ with f=1	estimated $\delta^{18}Ow$ with f=0.66
ES 16.62	Tortonien	Albox	between Albox and Saliente	Group of nodules-core of nodule 5	2.60	4.91	23.1	19.4				
ES 16.63	Tortonien	Albox	between Albox and Saliente	Gypsum veins					-4.5	5.5	-2.1	-7.4
ES 16.125	Tortonien II	Murcia	Camino de los Gonzalez	Group of nodules-core of nodule 1	1.29	7.26	29.6	25.6				
ES 16.126	Tortonien II	Murcia	Camino de los Gonzalez	Group of nodules-conduit intra nodules	-0.72	1.25	40.3	35.9				
ES 16.127	Tortonien II	Murcia	Camino de los Gonzalez	Gypsum vein					-21.3	2.5	-5.1	-11.9
ES 17-45	Tortonien	Murcia	Ginovinos, road RF-M 56	Nodule 2-central part	0.13	5.78	35.6	31.4				
ES 17-46	Tortonien	Murcia	Ginovinos, road RF-M 56	Gypsum vein around Nodule 2					-22.3	0.4	-7.2	-15.1
ES 17-64	Tortonian	Murcia	Ginovinos, road RF-M 56	Gypsum veins					-13.2	4.4	-3.2	-9.1
ES-94-5	Tortonian	Lorca	median part	layered dolomite	0.14	6.08	35.6	31.3				
ES-94-49	Tortonian	Lorca	median part	layered dolomite	0.08	4.59	35.9	31.7				
ES-94-46	Tortonian	Lorca	median part	layered dolomite	-0 ,06	3.64	32.4	28.3				
ES-94-39	Tortonian	Lorca	median part	layered dolomite	0.30	4.46	34.7	30.5				
ES-98.2-116	Tortonian	Lorca	median part	layered dolomite	-0.34	4.32	38.2	33.9				
ES-98.2-114	Tortonian	Lorca	median part	layered dolomite	-0.61	3.42	39.7	35.3				
ES-98-4	Tortonian	Lorca	median part	layered dolomite	-0.55	4.40	39.3	35.0				
ES-98.2 -80	Tortonian	Lorca	median part	layered dolomite	-0.07	4.79	36.7	32.4				
ES- 98 -2	Tortonian	Lorca	median part	layered dolomite	-0.39	4.39	38.4	34.1				
ES-98.2 -101	Tortonian	Lorca	median part	layered dolomite	-0.31	4.31	38.0	33.7				
ES-98 -3	Tortonian	Lorca	median part	layered dolomite	0.05	5.20	36.0	31.8				
ES-97-84	Tortonian	Lorca	median part	Gypsum veins					10.5	-2.2	-9.8	-19.1